

Research Article

Tension-Compression Damage Model with Consistent Crack Bandwidths for Concrete Materials

Wei He ¹, Ying Xu,¹ Yu Cheng ², Peng-Fei Jia ² and Ting-Ting Fu ³

¹School of Civil Engineering and Architecture, Anhui University of Science & Technology, Huainan, China

²Jiangsu Transportation Institute, Nanjing, China

³General Station of Construction Project Quality & Safety for Administration and Supervision, Jinhua, China

Correspondence should be addressed to Wei He; whe@aust.edu.cn

Received 29 August 2018; Revised 7 November 2018; Accepted 23 December 2018; Published 7 February 2019

Academic Editor: Giovanni Garcea

Copyright © 2019 Wei He et al. This is an open access article distributed under the Creative Commons Attribution License, which permits unrestricted use, distribution, and reproduction in any medium, provided the original work is properly cited.

This paper proposes a tension-compression damage model for concrete materials, formulated within the framework of thermodynamics of irreversible processes. The aim of this work is to solve the following problems: the premature divergence of numerical solutions under general loading conditions due to the conflict of tensile and compressive damage bounding surfaces, which is a result of the application of the spectral decomposition method to distinguish tension and compression, and the unsatisfactory reproduction of distinct tension-compression behaviors of concrete by strain-driven damage models. The former is solved by the sign of the volumetric deformation, while the latter is solved via two separated dissipation mechanisms. Moreover, of specific interest is an improved solution to the problem of mesh-size dependency using consistent crack bandwidths, which takes into account situations with irregular meshes and arbitrary crack directions in the context of the crack band approach. The performance of the model is validated by the well-documented experimental data. The simplicity and the explicit integration of the constitutive equations render the model well suitable for large-scale computations.

1. Introduction

Concrete is still one of the most widely used construction materials in civil engineering applications [1]. Therefore, developing an efficient constitutive model for concrete is of great importance since it contributes to engineering designs, failure analyses, and life-cycle assessments by reducing costs and time [2]. Microscopically, the mechanical behavior of concrete materials is mainly governed by the nucleation and growth of microcracks and their coalescence into macrocracks [3], which may result in the failure of a structure. Physically, it is an irreversible thermodynamic process accompanying energy dissipation and changes of the microstructure [4]. Such a progressive degradation of material properties can be phenomenologically described by models [5–17] based on continuum damage mechanics (CDM), which is generally accepted by the scientific and engineering communities [18].

Despite the achievements of CDM over a wide range of materials (e.g., [19–22]), the rational and accurate CDM

modeling of concrete materials still represents a challenging task. Three modeling challenges have been identified in finite element (FE) analyses. The first challenge is the criterion distinguishing tension and compression, which is used for activating/inactivating damage evolutions in tension and compression. The existing models usually utilize the spectral decomposition of a stress or strain tensor into tensile (positive) and compressive (negative) eigenvalues (e.g., [23, 24]), in order to describe different behaviors of concrete under general loading conditions. However, in the use of this method, the following problem would arise: divergence of numerical solutions will occur under biaxial or reverse loading conditions due to the conflict of tensile and compressive damage bounding surfaces induced by Poisson's ratio effect [25]. A better solution to this problem is the introduction of a weighted damage parameter (e.g., [5, 25]). Moreover, the sign of the volumetric strain ([26]) is used to distinguish what is tension and what is compression. However, it should be noted that the aforementioned method is

not applicable to incompressible materials which have a value of Poisson's ratio around 0.5 (e.g., fresh concrete and concrete under confinement) since the volumetric strain is null. Therefore, the present model is limited to the compressible materials characterized by Poisson's ratio lower than 0.5.

The second challenge is the modeling of tension-compression behaviors of concrete materials which exhibit large differences in their peak strengths and postpeak stages, as well as the unilateral effect characterized by a total or partial recovery of the degraded stiffness during the tension-compression load reversal. The classical strain-driven damage models incorporating one damage criterion alone may be incapable of predicting such distinct behaviors. Among them (e.g., [27–32]), one case can be mentioned as an example: the predicted strength of concrete under biaxial compression is seriously lower than that under uniaxial compression. To solve the problem, this paper proposes two separate damage criteria describing the state of damage under tension and compression, respectively, whereby the distinct behaviors can be reproduced in a physically realistic fashion. Due to the scope of this paper, the unilateral effect will not be discussed.

The third challenge is to avoid the lack of mesh objectivity of numerical results when the modeling of strain-softening is taken into account. At the stage of strain-softening, the concrete does not lose its entire load-carrying capacity but exhibits a progressively decreasing residual strength. Therefore, capturing the strain-softening is important because it is responsible for predicting the behavior of overloaded structures. However, damage models based on conventional continuum theories usually produce mesh-dependent results in FE analyses [6]. The mesh dependency can be further classified into mesh-size [33] and mesh-bias [34] dependencies. The mesh-size dependency, which originates from the loss of ellipticity of the governing partial differential equations for static problems [35], which means that both the computed energy dissipation due to strain-softening and the corresponding force-displacement response are governed by the fineness of the FE mesh [36]. It also reflects a physically unrealistic fact that the infinitesimal element size leads to a vanishing energy dissipation during the structural failure [37]. The mesh-bias dependency, which is a result of the inadequacy of the spatial discretization procedure [38, 39], means that the numerical result depends on the orientation of the FE mesh in the sense that the computed direction of the strain localization band tends to propagate along continuous mesh lines [40], which may give rise to spurious crack trajectories. Although the problem of mesh-bias dependency is important for damage modeling of concrete materials, this study focuses only on the solution to the mesh-size dependency.

To solve the problem of mesh-size dependency in the framework of continuum mechanics, various types of regularization methods have been developed that can be distinguished by the crack band approach (or fracture energy regularization) [33, 41, 42], nonlocal models including the

integral-type [6, 43, 44] and the gradient-type [13, 45], micropolar method [46], and viscous or rate-dependent [11] methods. On one hand, the nonlocal method seems to be more recent (e.g., [28, 30, 47]). However, the nonlocal models have their own difficulties such as (i) incorrect crack initiation, ahead of the crack tip [48], and (ii) incorrect shielding effect with nonzero nonlocal interactions across a crack surface [49]. Furthermore, nonlocal methods have no potential for large-scale computations of concrete structures since they require small enough elements, e.g., their sizes are at least one-third of the characteristic length of the material [50], to subdivide strain localization bands of the structure, which are usually a priori unknown. On the other hand, the crack band approach is widely used in most of the commercial FE packages and is still an important analytical tool for practical applications (e.g., [51, 52]). One goal of the present work is to propose a constitutive model which needs to ensure a high algorithmic efficiency and an easy implementation; therefore, a fracture energy regularization based on the crack band approach [33] is adopted.

One key parameter in the crack band approach is the crack bandwidth, through which the fracture energy (regarded to be a material property) is related to the volumetric (or specific) fracture energy, and it therefore ensures an objectivity of the energy dissipation regardless of the mesh refinement. The existing estimations of the crack bandwidth can be divided into three categories: (i) methods based on the square root of the element area (for two-dimensional elements) or the cubic root of the element volume (for three-dimensional elements) (e.g., [53–55]); (ii) the notable methods proposed by Oliver [56]; and (iii) projection methods (e.g., [57–60]). The methods in the first category, which estimate the crack bandwidth as a constant during the numerical analysis process, are less applicable to situations with irregular meshes or arbitrary crack directions [56]. The methods in the last two categories, in which crack bandwidths are varied with respect to crack directions and spatial positions, solve the aforementioned problems. However, they may encounter difficulties such as excessively large estimation [59] or misprediction of the crack bandwidth. This paper therefore develops an improved estimation of the crack bandwidth to circumvent the above difficulties. Moreover, two different crack bandwidths (one for the tensile strain-softening and the other for the compressive strain-softening) are taken into account in the present study, because of which concrete exhibits quite different localization behaviors in tension and compression [61]. It should also be noted that the crack band approach can only be regarded as a partial regularization method for mesh-size dependency in the sense that the objectivity of the energy dissipation is ensured [62], and thus the global structural response can be captured correctly [56], but the mathematical description of the rate boundary value problem (BVP) still remains ill-posed [63].

The main purpose of this study is not to describe all the mechanical behaviors of concrete but rather to give methodological efforts to solve the aforementioned difficulties. Therefore, the plastic dissipation is not considered and the isotropic damage is assumed for simplification. Accordingly,

the objectives of this paper are fourfold: (i) to define the criterion distinguishing tension and compression by the sign of the volumetric deformation; (ii) to propose a model to describe distinct tension-compression behaviors of concrete materials under a framework similar to that of Cervera et al. [11] and Comi and Perego [26]; (iii) to develop an improved estimation of the crack bandwidth using the projection method for solving the problem of mesh-size dependency; and (iv) to validate the proposed model by the selected benchmark tests.

2. Tension-Compression Damage Model with Consistent Crack Bandwidths

2.1. Helmholtz Free Energy Potential. The thermodynamics of irreversible processes provides a general framework for formulating constitutive equations. In other words, the state of the material can be described by the thermodynamic potential. Consequently, the stresses and other associated variables can be derived from this potential [64]. Because of the scope of this paper, the present model is developed based on the following assumptions: (i) damage evolutions are assumed to be isotropic and to occur in small strains and (ii) the rate-dependent behavior and the thermal effect are not considered. To take into account distinct tension-compression behaviors of concrete, the postulated thermodynamic potential in terms of Helmholtz free energy ψ is decomposed into volumetric and deviatoric parts ψ_v and ψ_d in a similar way as in the study of Cervera et al. [11] and Comi and Perego [26] as follows:

$$\begin{aligned} \rho\psi(\boldsymbol{\varepsilon}, d_t, d_c) &= \rho\psi_v(\boldsymbol{\varepsilon}_v, d_t, d_c) + \rho\psi_d(\boldsymbol{\varepsilon}_d, d_t, d_c) \\ &= \rho\psi_v^+(\boldsymbol{\varepsilon}_v^+, d_t, d_c) + \rho\psi_v^-(\boldsymbol{\varepsilon}_v^-, d_t, d_c) \\ &\quad + \rho\psi_d(\boldsymbol{\varepsilon}_d, d_t, d_c), \end{aligned} \quad (1)$$

$$\rho\psi_v^+(\boldsymbol{\varepsilon}_v^+, d_t, d_c) = \frac{3}{2}(1-d_t)(1-d_c)K_0\boldsymbol{\varepsilon}_v^+ : \boldsymbol{\varepsilon}_v^+, \quad (2)$$

$$\rho\psi_v^-(\boldsymbol{\varepsilon}_v^-, d_t, d_c) = \frac{3}{2}(1-d_c)K_0\boldsymbol{\varepsilon}_v^- : \boldsymbol{\varepsilon}_v^-,$$

$$\rho\psi_d(\boldsymbol{\varepsilon}_d, d_t, d_c) = [1 - H(\text{tr}\boldsymbol{\varepsilon})d_t][1 - H(-\text{tr}\boldsymbol{\varepsilon})d_c]G_0\boldsymbol{\varepsilon}_d : \boldsymbol{\varepsilon}_d, \quad (3)$$

where ρ is the mass density of the material, $\boldsymbol{\varepsilon}$ is the second-order strain tensor, d_t and d_c are the damage internal variables that represent the level of material degradation in tension and compression, K_0 and G_0 are the initial bulk and shear moduli of the undamaged material, respectively, $H(\bullet)$ is the Heaviside function defined by $H(x) = 1$ if $x \geq 0$ and $H(x) = 0$ if $x < 0$, and $\text{tr}(\bullet)$ is the trace of a tensor. The tensile and compressive damage internal variables are monotonously increasing scalars, both of which grow from zero (undamaged material with the intact stiffness) to one (completely damaged material). $\boldsymbol{\varepsilon}_v$ and $\boldsymbol{\varepsilon}_d$ are second-order volumetric and deviatoric strain tensors, defined by the following equation:

$$\boldsymbol{\varepsilon}_v = \mathbb{I}_v : \boldsymbol{\varepsilon}, \quad (4)$$

$$\boldsymbol{\varepsilon}_d = \mathbb{I}_d : \boldsymbol{\varepsilon}, \quad (5)$$

$$\mathbb{I}_v = \frac{1}{3}\mathbf{I} \otimes \mathbf{I}, \quad (6)$$

$$\mathbb{I}_d = \mathbb{I}_s - \mathbb{I}_v, \quad (7)$$

where \mathbb{I}_v and \mathbb{I}_d are the fourth-order volumetric and deviatoric projections, respectively, and \mathbf{I} and \mathbb{I}_s are the second-order identity tensor and the fourth-order symmetric identity tensor, respectively.

$\boldsymbol{\varepsilon}_v^+$ and $\boldsymbol{\varepsilon}_v^-$ are positive and negative volumetric strain tensors, defined according to

$$\boldsymbol{\varepsilon}_v^+ = H(\text{tr}\boldsymbol{\varepsilon})\boldsymbol{\varepsilon}_v, \quad (8)$$

$$\boldsymbol{\varepsilon}_v^- = H(-\text{tr}\boldsymbol{\varepsilon})\boldsymbol{\varepsilon}_v. \quad (9)$$

2.2. Damage Criteria. To describe the damage due to tension or compression, it first necessitates a criterion that defines tensile/compressive states. As mentioned in Introduction, the method of spectral decomposition may lead to the premature convergence problem in numerical solutions [25]. Therefore, the sign of the volumetric deformation (relative volume change), which is calculated by $\text{tr}\boldsymbol{\varepsilon}$, is used to distinguish tension and compression in this paper. The similar application can be found in the work of Comi and Perego [26]. In the following, the tensile and compressive strain states are thus defined by $\text{tr}\boldsymbol{\varepsilon} \geq 0$ and $\text{tr}\boldsymbol{\varepsilon} < 0$, respectively.

The damage criterion characterizes the state of damage and represents a bounding surface whose boundary corresponds to the states at which the damage will grow. To clearly specify the damage due to tension or compression, two damage criteria are introduced as follows:

$$F_i(\varepsilon_i^{\text{eq}}, \kappa_i) = \varepsilon_i^{\text{eq}}(\boldsymbol{\varepsilon}) - \kappa_i \leq 0, \quad (i = t \text{ or } c), \quad (10)$$

where F_t and F_c are the tensile and compressive damage criteria, $\varepsilon_t^{\text{eq}}$ and $\varepsilon_c^{\text{eq}}$ are the equivalent tensile and compressive strains, and κ_t and κ_c are the current tensile and compressive damage thresholds, respectively. It is noteworthy that the damage does not develop if $F_i < 0$ and grows if $F_i = 0$.

The damage threshold represents the largest value of the equivalent strain ever reached by the material during the loading history [65–67]. Therefore, κ_t and κ_c can be further expressed as follows:

$$\kappa_i(t) = \max_{\tau \leq t}(\varepsilon_i^{\text{eq}}(\tau)), \quad (i = t \text{ or } c). \quad (11)$$

Similar to the work of Fichant et al. [68], the equivalent strains in equation (10) are assumed to be as follows:

$$\varepsilon_i^{\text{eq}} = \frac{1}{E_0}(\alpha_i I_{1\sigma} + \beta_i \sqrt{J_{2\sigma}}), \quad (i = t \text{ if } \text{tr}\boldsymbol{\varepsilon} \geq 0, i = c \text{ otherwise}), \quad (12)$$

with

$$I_{1\sigma} = \text{tr}\sigma_e, \quad (13)$$

$$J_{2\sigma} = \frac{1}{2}\sigma_e : \sigma_e - \frac{1}{6}I_{1\sigma}^2,$$

$$\sigma_e = \mathbb{C}_0 : \boldsymbol{\varepsilon},$$

$$\alpha_t = \frac{1}{2} \left(1 - \frac{f_t}{f_c} \right),$$

$$\beta_t = \frac{\sqrt{3}}{2} \left(1 + \frac{f_t}{f_c} \right),$$

$$\alpha_c = 1 - \frac{f_c}{f_{bc}},$$

$$\beta_c = \sqrt{3} \left(2 - \frac{f_c}{f_{bc}} \right), \quad (14)$$

where E_0 is the initial Young's modulus of the undamaged material, $I_{1\sigma}$ is the first invariant of the effective stress tensor, $J_{2\sigma}$ is the second invariant of the deviatoric effective stress tensor, σ_e is the effective stress tensor, \mathbb{C}_0 is the fourth-order elastic stiffness tensor of the undamaged material, α_i and β_i are the material constants, f_t is the uniaxial tensile strength, and f_c and f_{bc} are the uniaxial and biaxial compressive strengths of the material, respectively. Following the experimental result from the study of Kupfer et al. [69], the typical value of $f_{bc}/f_c = 1.16$ for concrete is adopted throughout this paper.

2.3. Evolution Laws for Internal Variables. From the macroscopic viewpoint within the framework of thermodynamics, the damage variable can be introduced as an internal state variable to quantify the average material degradation [22]. In order to capture distinct tension-compression behaviors of concrete, two types of damage evolution laws, which relate the corresponding damage internal variable to the associated damage threshold, are defined in the following general form:

$$d_i = g_i(\kappa_i), \quad (i = t \text{ or } c). \quad (15)$$

In this paper, explicit damage evolution laws are further postulated as follows:

$$d_t = g_t(\kappa_t) = \begin{cases} 0, & \text{if } \kappa_t \leq \kappa_t^0, \\ 1 - \frac{\kappa_t^0}{\kappa_t} \left(\frac{\kappa_t^u - \kappa_t}{\kappa_t^u - \kappa_t^0} \right)^{A_t}, & \text{if } \kappa_t^0 < \kappa_t < \kappa_t^u, \\ 1, & \text{if } \kappa_t \geq \kappa_t^u, \end{cases} \quad (16)$$

$$d_c = g_c(\kappa_c) = \begin{cases} 1 - \frac{1}{1 + (\gamma - 1)(\kappa_c/\kappa_c^0)^{(\gamma/\gamma-1)}}, & \text{if } \kappa_c \leq \kappa_c^0, \\ 1 - \frac{\kappa_c^0}{\gamma\kappa_c} \left[1 - \left(\frac{\kappa_c - \kappa_c^0}{\kappa_c^u - \kappa_c^0} \right)^2 \right], & \text{if } \kappa_c^0 < \kappa_c < \kappa_c^u, \\ 1, & \text{if } \kappa_c \geq \kappa_c^u, \end{cases} \quad (17)$$

where $\kappa_t^0 = f_t/E_0$ and $\kappa_c^0 = \gamma f_c/E_0$ are the initial tensile and compressive damage thresholds, respectively, with γ being the material parameter. A_t is the nonnegative material parameter that controls the shape of the tensile stress-strain relation, as shown in Figure 1. It is noteworthy that if $A_t = 1$, then the damage evolution law in tension represents a linear softening. κ_t^u and κ_c^u are the ultimate tensile and compressive damage thresholds, respectively. According to the crack band approach [33], the ultimate damage threshold depends on the fracture energy and the crack bandwidth. It will be further discussed later.

At any material point, damage can evolve only if the current state reaches the boundary of the elastic domain, characterized by $F_i(\varepsilon_i^{\text{eq}}, \kappa_i) = 0$. To reflect the loading, unloading, and reloading conditions more generally, the evolution of damage internal variables is governed by the following Kuhn–Tucker relations:

$$F_i(\varepsilon_i^{\text{eq}}, \kappa_i) \leq 0, \quad \dot{d}_i \geq 0, \quad (18)$$

$$F_i(\varepsilon_i^{\text{eq}}, \kappa_i) \dot{d}_i = 0, \quad (i = t \text{ or } c).$$

2.4. Mechanical Dissipation and Constitutive Laws. The failure of concrete is related to the degradation of physical properties of the material. During this damage process, the energy dissipation is always nonnegative and accompanied by an increase of entropy [66]. It hence implies an irreversible process of thermodynamics. Therefore, the mechanical dissipation ϕ_d under the isothermal condition needs to satisfy the second principle of thermodynamics, which can be expressed by the Clausius–Duhem inequality as follows:

$$\dot{\phi}_d = \boldsymbol{\sigma} : \dot{\boldsymbol{\varepsilon}} - \rho \dot{\psi} \geq 0, \quad (19)$$

where $\boldsymbol{\sigma}$ is the second-order stress tensor.

Substitution of equation (1) into equation (19) yields the following equation:

$$\dot{\phi}_d = \left(\boldsymbol{\sigma} - \rho \frac{\partial \psi}{\partial \boldsymbol{\varepsilon}} \right) : \dot{\boldsymbol{\varepsilon}} + Y_t \dot{d}_t + Y_c \dot{d}_c \geq 0, \quad (20)$$

with the tensile and compressive damage energy release rates defined as follows:

$$Y_i = -\rho \frac{\partial \psi}{\partial d_i} = -\frac{1}{2} \boldsymbol{\varepsilon} : \frac{\partial \mathbb{C}}{\partial d_i} : \boldsymbol{\varepsilon}, \quad (i = t \text{ or } c), \quad (21)$$

where \mathbb{C} is the fourth-order secant stiffness tensor of the damaged material.

Because of the fact that the inequality of equation (20) must be satisfied by the arbitrary change of the strain tensor $\boldsymbol{\varepsilon}$, the coefficient of the first term of the inequality, therefore, must be zero. This requirement yields the following constitutive laws:

$$\boldsymbol{\sigma} = \rho \frac{\partial \psi}{\partial \boldsymbol{\varepsilon}}, \quad (22)$$

$$\mathbb{C}(d_t, d_c) = \frac{\partial \boldsymbol{\sigma}}{\partial \boldsymbol{\varepsilon}} = \rho \frac{\partial^2 \psi}{\partial \boldsymbol{\varepsilon} \partial \boldsymbol{\varepsilon}}. \quad (23)$$

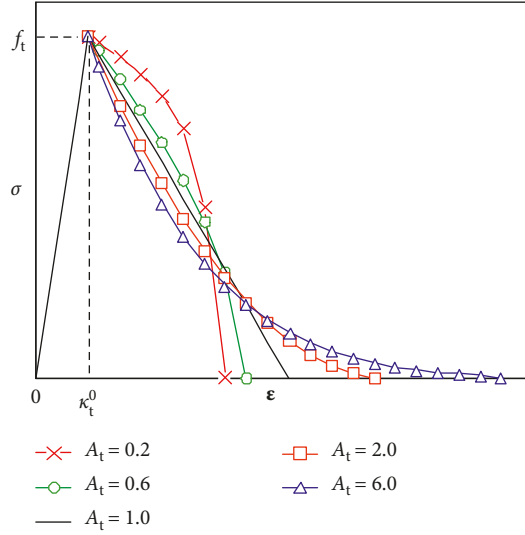


FIGURE 1: Influence of A_t on uniaxial stress-strain relation in tension.

Using equation (22), the Clausius–Duhem inequality expressed by equation (20) is eventually written in the following form:

$$\dot{\phi}_d = Y_t \dot{d}_t + Y_c \dot{d}_c \geq 0. \quad (24)$$

Therefore, the second principle of thermodynamics is satisfied as long as the damage variables d_t and d_c are monotonically increasing since Y_t and Y_c are strictly non-negative because of their quadratic forms, which involve $\partial C / \partial d_i \leq 0$.

2.5. Fracture Energy Regularization with Consistent Crack Bandwidths. To solve the problem of mesh-size dependency, a fracture energy regularization based on the crack band approach [33] is adopted in the present study. The general idea of the crack band approach is to rescale the softening branch of the stress-strain curve, in order to impose the same energy dissipation per unit area for different element sizes [59]. This adjustment consists in relating the fracture energy (regarded to be a material property) to the volumetric (or specific) fracture energy (Figures 2(c) and 2(d)), which depends on the crack bandwidth. To achieve this goal of regularization, it is finally required to relate the ultimate damage threshold to the fracture energy and the crack bandwidth.

The crack band approach assumes that the failure of material occurs within a damage zone having a limited width, whereas the other parts are unloaded [59] during the process of failure (Figure 2). According to Bažant and Oh [33] and Jirásek and Marfia [43], the same energy dissipation per unit area can be ensured using following relations:

$$G_t^f = l_t^{(P)} g_t^f = l_t^{(P)} \int_0^{\kappa_t^u} \sigma_t^{mn}(\kappa_t) d\kappa_t, \quad (25)$$

$$G_c^f = l_c^{(P)} g_c^f = l_c^{(P)} \int_{\kappa_c^0}^{\kappa_c^u} \sigma_c^{mn}(\kappa_c) d\kappa_c, \quad (26)$$

where G_t^f and G_c^f are the Mode-I and compressive fracture energies defined as the energy dissipation per unit area of a

surface due to cracking or crushing, $l_t^{(P)}$ and $l_c^{(P)}$ are the tensile and compressive crack bandwidths, g_t^f and g_c^f are the tensile and compressive volumetric fracture energies defined as the energy dissipation per unit volume, and σ_t^{mn} and σ_c^{mn} are the tensile and compressive stresses normal and tangential to the surface of cracking, respectively. It is noteworthy that G_t^f and g_t^f can be represented by the area under the traction-separation (tensile stress normal to the crack versus crack opening displacement) curve and under the stress-strain curve, respectively, as shown in Figures 2(c) and 2(d).

Using equation (16), substitution of equation (22) into equation (25) yields the following equation:

$$\kappa_t^u = \frac{(1 + A_t)G_t^f}{l_t^{(P)} f_t} + \frac{1 - A_t}{2} \kappa_t^0. \quad (27)$$

It is noteworthy that equation (27) is derived under the condition of uniaxial loading. Nevertheless, the previous studies (e.g., [20, 70, 71]) have revealed that it is also an acceptable approximation under general loading conditions.

Similarly, the compressive damage threshold κ_c^u can be expressed as follows:

$$\kappa_c^u = \frac{3}{2} \frac{G_c^f}{l_c^{(P)} f_c} + \kappa_c^0. \quad (28)$$

Generally, the crack bandwidth can be regarded as an FE discretization parameter, which depends on the chosen element shape (e.g., quadrilaterals or triangles), element size, element orientation (or mesh alignment) with respect to the direction of the strain localization band, interpolation function or order of the displacement approximation (e.g., linear or quadratic), and numerical integration scheme (number of integration points) [53, 59, 60]. For the sake of simplicity, only four-node quadrilateral and three-node triangular elements are used throughout the paper. It should also be noted that only low-order elements (i.e., elements with linear or multi-linear interpolation functions) are adopted in this study since the stress fields obtained from high-order elements (i.e., elements with quadratic interpolation functions) are highly disturbed for crack band simulations [59].

Inspired by the works of Červenka et al. [57] and Jirásek and Bauer [59], this paper develops an improved estimation of crack bandwidths in tension and compression by projecting the element onto the directions normal and tangential to the crack direction, respectively. Mathematically, they can be written as follows:

$$l_i^{(P)} = |l_i^{\max} - l_i^{\min}| \quad (i = t \text{ or } c), \quad (29)$$

with

$$l_t^{\max} = \max_{N=1, N_{m-n}} [\mathbf{x}_N \cdot \mathbf{n}(\mathbf{x})],$$

$$l_t^{\min} = \min_{N=1, N_{m-n}} [\mathbf{x}_N \cdot \mathbf{n}(\mathbf{x})], \quad (30)$$

$$l_c^{\max} = \max_{N=1, N_{m-n}} [\mathbf{x}_N \cdot \mathbf{t}(\mathbf{x})],$$

$$l_c^{\min} = \min_{N=1, N_{m-n}} [\mathbf{x}_N \cdot \mathbf{t}(\mathbf{x})], \quad (31)$$

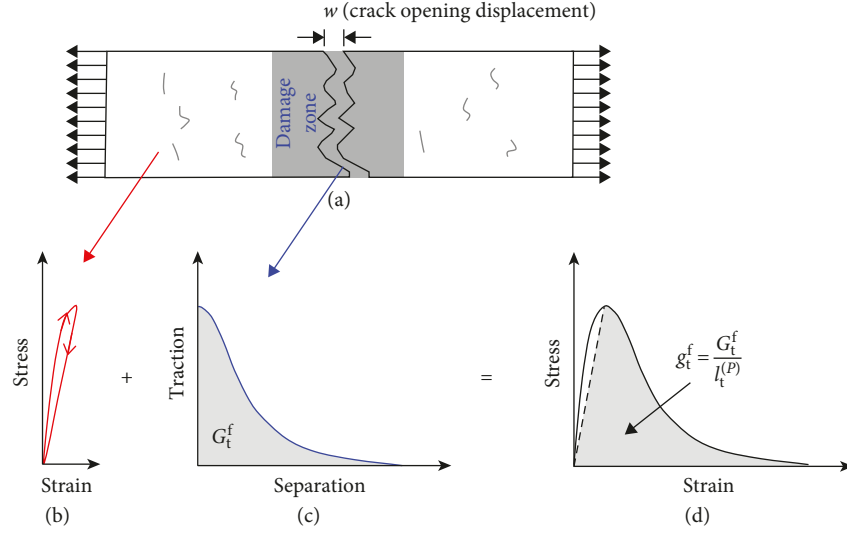


FIGURE 2: Damage zone and fracture energy regularization: (a) damage zone in the concrete specimen under tensile loading; (b) stress-strain response outside the damage zone; (c) traction-separation law in the damage zone; (d) general stress-strain relation for the concrete specimen.

where $l_t^{(P)}$ and $l_c^{(P)}$ are the tensile and compressive crack bandwidths, l_i^{\max} and l_i^{\min} ($i = t$ or c) are the maximum and minimum projection values, \mathbf{x}_N is the midpoint of the element edge (for four-node quadrilateral elements) or the nodal point (for three-node triangular elements), N_{m-n} is the number of element midpoints (for four-node quadrilateral elements) or nodes (for three-node triangular elements), \mathbf{x} represents the point (e.g., Gaussian point) in the structure where the crack bandwidth is to be evaluated, and $\mathbf{n}(\mathbf{x})$ and $\mathbf{t}(\mathbf{x})$ are the unit vectors with the direction normal and tangential to the crack direction at the point \mathbf{x} , respectively. The geometrical meaning of equation (29) is illustrated in Figure 3.

For comparison, the existing estimation formulas of the crack bandwidth mentioned in Introduction are recalled as follows.

The tensile crack bandwidth $l_t^{(R)}$, which is estimated by Rots [53] belonging to the first category, can be written as follows:

$$l_t^{(R)} = \begin{cases} \sqrt{A}, & \text{for quadratic two-dimensional elements,} \\ \sqrt{2A}, & \text{for linear two-dimensional elements,} \end{cases} \quad (32)$$

with A being the area of the element.

The tensile crack bandwidth $l_t^{(O)}$, which is estimated according to the first method of Oliver [56], can be expressed as follows:

$$l_t^{(O)} = \left[\left(\sum_{i=1}^{N_c} \phi_i \frac{\partial N_i(\mathbf{x})}{\partial \mathbf{x}} \right) \cdot \mathbf{n}(\mathbf{x}) \right]^{-1}, \quad (33)$$

with

$$\phi_i = \begin{cases} 1, & \text{if } (\mathbf{x}_i - \mathbf{x}_c) \cdot \mathbf{n}(\mathbf{x}) \geq 0, \\ 0, & \text{if } (\mathbf{x}_i - \mathbf{x}_c) \cdot \mathbf{n}(\mathbf{x}) < 0, \end{cases} \quad (34)$$

where N_c is the number of corner nodes of the element, N_i is the standard shape function for the corner node i belonging to an element with N_c corner nodes, ϕ_i is the nodal value at the corner node i , and \mathbf{x}_i and \mathbf{x}_c are the corner node and the center of the element, respectively.

The tensile crack bandwidth $l_t^{(G)}$, which is estimated by Govindjee et al. [58] belonging to the third category, can be given as follows:

$$l_t^{(G)} = \left[\left(\sum_{i=1}^{N_c} \tau_i \frac{\partial N_i(\mathbf{x})}{\partial \mathbf{x}} \right) \cdot \mathbf{n}(\mathbf{x}) \right]^{-1}, \quad (35)$$

with

$$\tau_i = \frac{(\mathbf{x}_i - \mathbf{x}_c) \cdot \mathbf{n}(\mathbf{x}) - \tau^{\min}}{\tau^{\max} - \tau^{\min}}, \quad (36)$$

$$\tau^{\max} = \max_{i=1, N_c} [(\mathbf{x}_i - \mathbf{x}_c) \cdot \mathbf{n}(\mathbf{x})],$$

$$\tau^{\min} = \min_{i=1, N_c} [(\mathbf{x}_i - \mathbf{x}_c) \cdot \mathbf{n}(\mathbf{x})]. \quad (37)$$

The geometrical meanings of the aforementioned tensile crack bandwidths and their differences with respect to the direction of $\mathbf{n}(\mathbf{x})$ are illustrated in Figures 4 and 5, where θ is the angle between the normal to the crack and the global axis x at the point \mathbf{x} . The crack bandwidths denoted by $l_t^{(O)}$ (according to equation (33)) become very large (Figures 4(b) and 5(b)) under certain circumstances, and they also show a discontinuity (Figures 4(c) and 5(c)), while the crack bandwidths denoted by $l_t^{(P)}$ and $l_t^{(G)}$ (according to equations (29) and (35), respectively) are free from such problems. The discontinuous crack bandwidth obtained from equation (33) is caused by the discontinuous nature of ϕ_i , whose value is either 1 or 0 as defined by equation (34). It is also noteworthy that the present method (labelled as $l_t^{(P)}$) and the method of Govindjee et al. [58] (labelled as $l_t^{(G)}$) give exactly the same

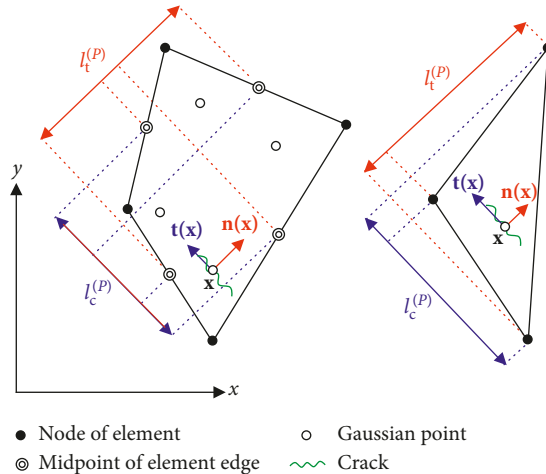


FIGURE 3: Proposed estimation of crack bandwidths.

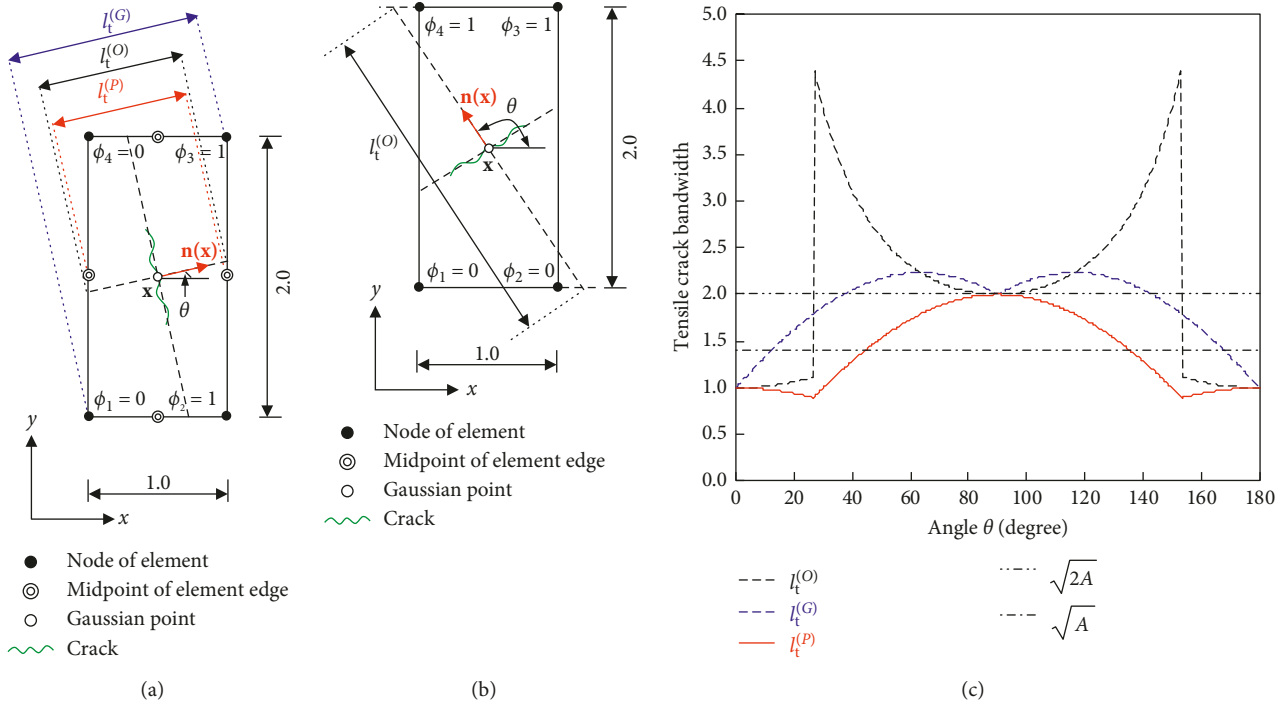


FIGURE 4: Comparison of estimations of crack bandwidth for a rectangular quadrilateral element: (a) geometrical meanings of crack bandwidths estimated by the present model, Oliver [56], and Govindjee et al. [58]; (b) large crack bandwidth estimated by the first method of Oliver [56]; (c) relations of tensile crack bandwidth and angle θ .

estimation of the tensile crack bandwidth for the linear triangular element as shown in Figures 5(a) and 5(c) since both of them use the method of projecting corner nodes of the element onto the direction normal to the crack direction. The further comparative study of these estimation methods will be given in the next section.

3. Model Verification

To establish the validity of the proposed constitutive model, the computed results were either verified theoretically or compared with measured ones from experiments. These are presented in the following sections.

3.1. Analysis of Biaxial Tests of Concrete. To examine the rationality of the adopted criterion distinguishing tension and compression, and to validate the present model in reproducing the distinct strength features of concrete under biaxial stresses, a series of plain concrete specimens subjected to different stress ratios (denoted by α), which were tested by Kupfer et al. [69], were chosen for the numerical analysis. The material properties used for the computation were Young's modulus $E_0 = 3.2 \times 10^4$ MPa, Poisson's ratio $\nu_0 = 0.2$, concrete uniaxial tensile strength $f_t = 3.28$ MPa, $A_t = 1.0$, uniaxial compressive strength $f_c = 32.8$ MPa, $\gamma = 2.3$, Mode-I fracture energy $G_t^f = 0.1$ N/mm, and compressive fracture energy $G_c^f = 15.0$ N/mm. A one-element

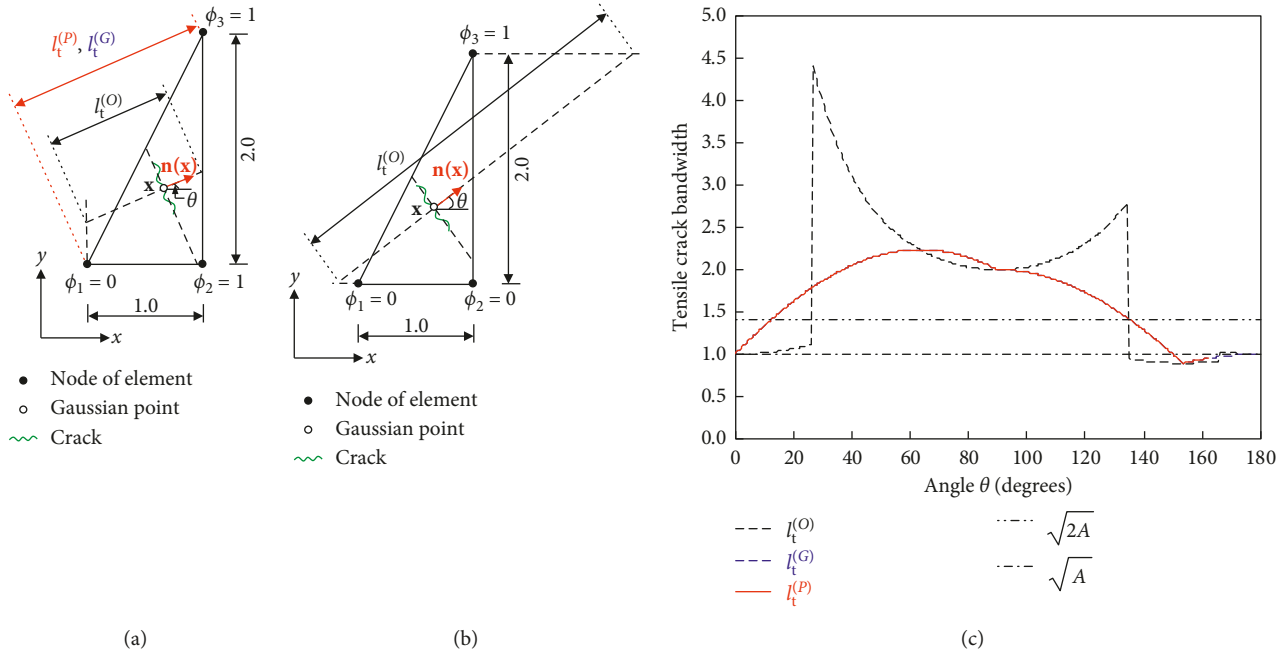


FIGURE 5: Comparison of estimations of crack bandwidth for a right triangular element: (a) geometrical meanings of crack bandwidths estimated by the present model, Oliver [56], and Govindjee et al. [58]; (b) large crack bandwidth estimated by the first method of Oliver [56]; (c) relations of tensile crack bandwidth and angle θ .

mesh (Mesh A was 200.0 mm long \times 200.0 mm high) with a four-node plane stress quadrilateral element using a 2×2 Gaussian integration scheme [44] was used to represent the plain concrete specimen (Figure 6).

Figure 6 shows the comparison between the experimental and computed results of the strength envelope, which corresponds to the envelope of the maximum stress ever reached in the material during the loading, in a biaxial principal stress space. The results indicate that the predicted biaxial strengths of concrete are very close to the experimental ones, either in the biaxial tensile domain or in the biaxial compressive domain, or even in the tensile-compressive domain. The numerical results in Figure 6 also demonstrate the rationality of the adopted criterion distinguishing tension and compression. Figure 7 shows the comparison of stress-strain curves of numerical and experimental results [69] under biaxial compression ($\sigma_3 = 0$), according to the following stress ratios ($\alpha = \sigma_2/\sigma_1$): $\alpha = 0$, $\alpha = 0.52$, and $\alpha = 1$. It shows that the proposed model can predict well both the strength enhancement of concrete and the corresponding peak strain in biaxial compressive states.

3.2. Analysis of a Double-Edge Notched Concrete Specimen under Direct Tension. To validate the proposed model in capturing the strain-softening, a double-edge notched (DEN) concrete specimen under direct tension, which was investigated experimentally by Hordijk [72], was used for the numerical analysis. The test specimen shown in Figure 8, which had dimensions 125 mm height \times 60 mm width \times 50 mm thickness with two symmetrical notches of $5 \times 5 \text{ mm}^2$ in the middle cross-section, was glued to the loading platens

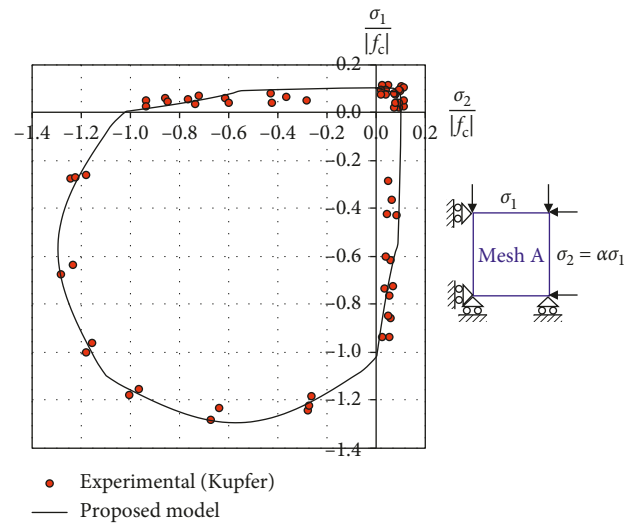


FIGURE 6: Biaxial strength envelope of concrete.

and subjected to an axial tensile load under the deformation control. The average deformation δ , which denotes the elongation of the specimen, was measured experimentally by using four pairs of extensometers located at the front and rear faces of the specimen. The gauge length of extensometers was 35 mm (Figure 8). The average stress σ_{avg} in the experiment was defined as the vertical load divided by the net cross-sectional area ($50 \times 50 \text{ mm}^2$).

The material properties of the test specimen used for the numerical analysis were Young's modulus $E_0 = 1.8 \times 10^4 \text{ MPa}$, Poisson's ratio $\nu_0 = 0.2$, concrete uniaxial tensile strength $f_t = 3.5 \text{ MPa}$, $A_t = 6.0$, uniaxial

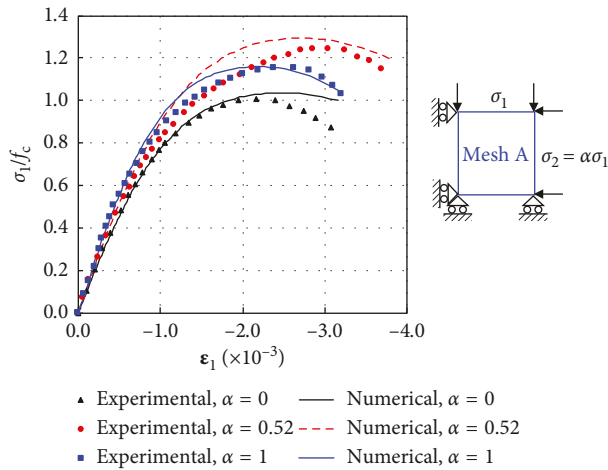


FIGURE 7: Computed stress-strain curves of concrete under biaxial compression.

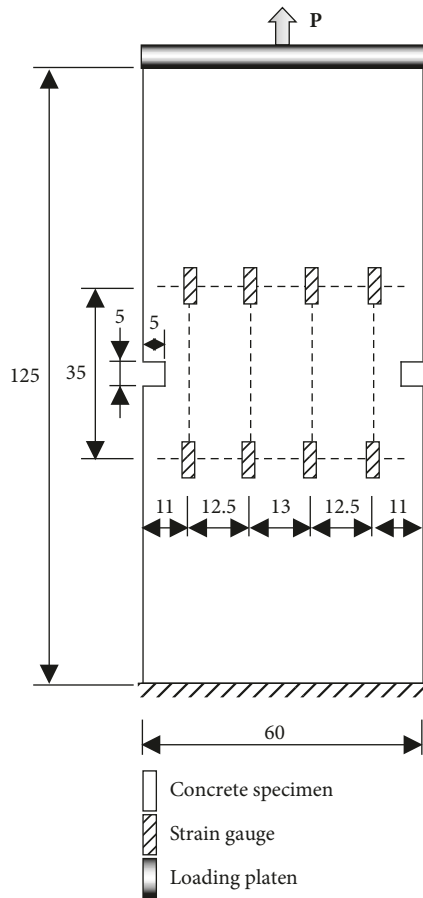


FIGURE 8: DEN concrete specimen: geometry, boundary, and loading conditions (dimensions in mm).

compressive strength $f_c = 34.0$ MPa, and Mode-I fracture energy $G_t^I = 0.07$ N/mm.

The DEN concrete specimen was modeled by a 298-element mesh with four-node plane stress quadrilateral elements using a 2×2 Gaussian integration scheme, as shown in Figure 9.

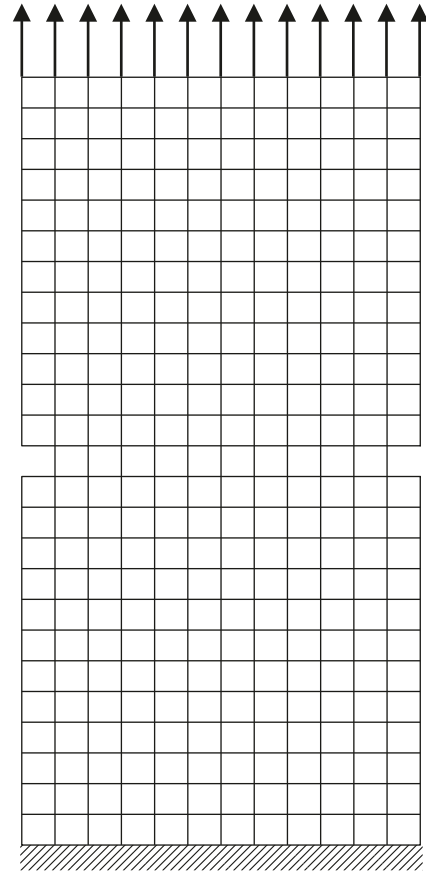


FIGURE 9: FE mesh for the DEN concrete specimen.

the experiment, all FE nodes at the lower boundary were assumed to be fixed (Figure 9). Figure 10 presents the computed average stress-deformation curve in tension. The numerical result shows a satisfactory agreement with the experimental one, including both the load-carrying capacity and the postpeak behavior.

3.3. Analysis of a Bar Subjected to Uniaxial Tension Using Elements with a Constant Strain Field. To prove the efficiency of the proposed estimation of the crack bandwidth with respect to the FE mesh irregularity, a bar subjected to uniaxial tension was used for the numerical analysis by following the work of Oliver [56]. Figure 11 shows the geometry, boundary, and loading conditions of the bar with a thickness of 50 mm.

The material properties used for the numerical analysis were Young's modulus $E_0 = 2.0 \times 10^4$ MPa, Poisson's ratio $\nu_0 = 0.0$, concrete uniaxial tensile strength $f_t = 2.0$ MPa, $A_t = 1.0$, uniaxial compressive strength $f_c = 20.0$ MPa, and Mode-I fracture energy $G_t^I = 0.1$ N/mm.

According to Oliver [56], the localization of the bar due to strain-softening was induced artificially by the prescribed imperfection (Figure 11) with a small reduction of the uniaxial tensile strength in shaded elements, as shown in Figure 12.

The bar was discretized by the four-node quadrilateral or three-node triangular plane stress elements, both of which

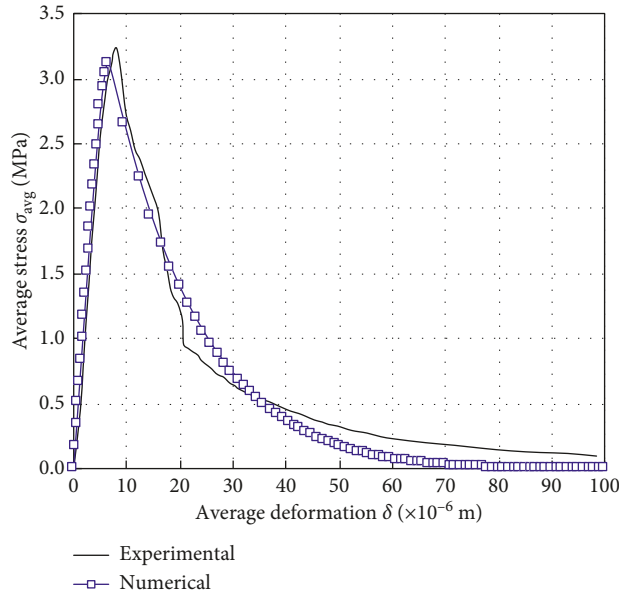


FIGURE 10: Average stress-deformation curves for the DEN concrete specimen.

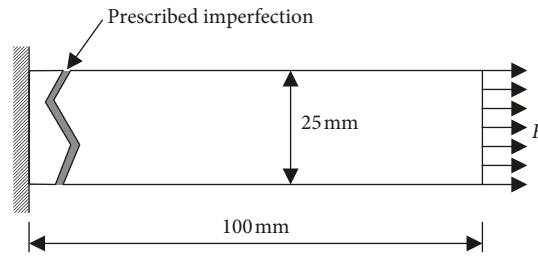


FIGURE 11: A bar subjected to uniaxial tension.

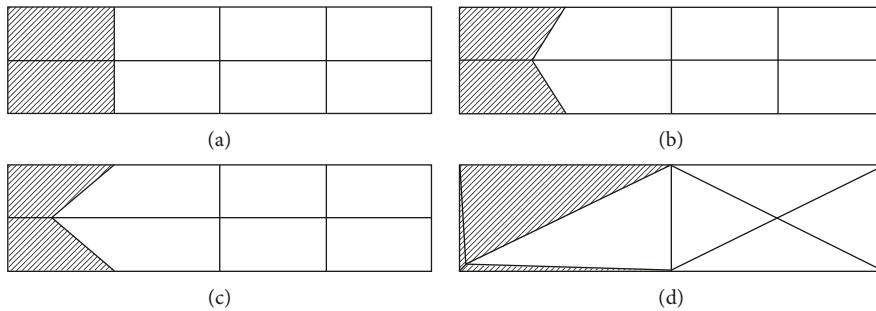


FIGURE 12: FE meshes used for the study of mesh irregularity (after the study [56]): (a) Mesh A; (b) Mesh B; (c) Mesh C; (d) Mesh D.

adopted a linear interpolation function (implying a constant strain field) and a 1-point Gaussian integration scheme. Figure 12 shows the meshes used for the analysis with different mesh irregularities.

Due to the fact that the projection methods (e.g., the present method and that of [58]) have solved the difficulty of the excessively large estimation of the crack bandwidth arising in the first method of Oliver [56] shown in the previous section, only the element area-based, Govindjee et al. [58]-based, and the present methods of estimating the crack bandwidth are compared in this section.

Figure 13(c) shows that the load-displacement responses obtained by the present method are almost coincident with the theoretical solution and are hardly detectable in the plots, while the corresponding responses, which were obtained by the crack bandwidth estimated by $\sqrt{2A}$ and by Govindjee et al. [58] using equation (35), show an unacceptable mesh dependency with respect to the FE mesh irregularity. Consequently, the present model provides an accurate estimation of the crack bandwidth that yields mesh-size independent results with respect to the mesh irregularity.

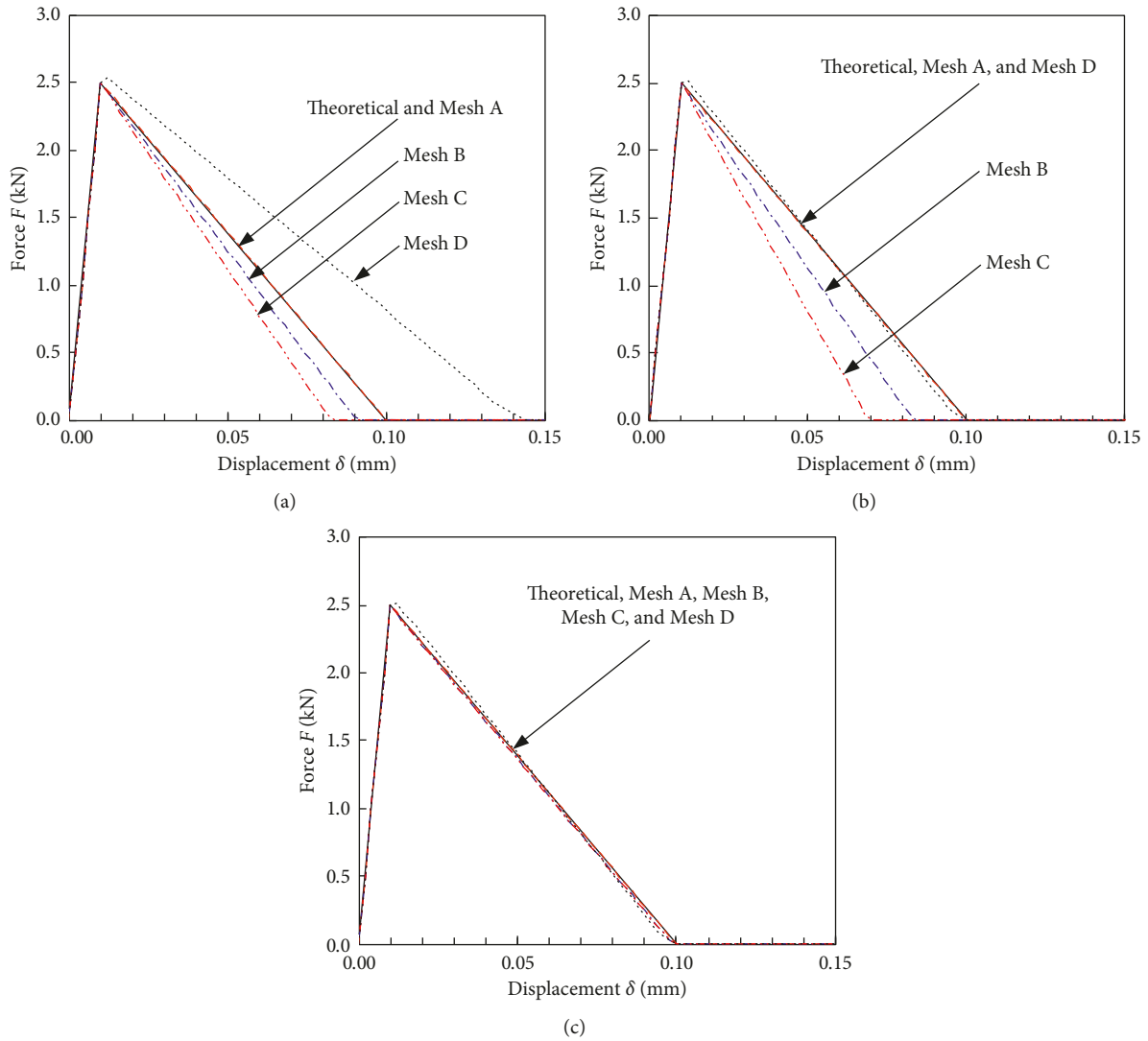


FIGURE 13: Force-displacement responses obtained by different estimations of crack bandwidth with different mesh irregularities: crack bandwidth estimated by (a) $\sqrt{2A}$, (b) Govindjee et al. [58], and (c) the present model.

3.4. Analysis of a Single-Edge Notched Concrete Beam Subjected to Four-Point Shear Loading. To demonstrate the mesh-size objectivity and the capability of the proposed model in predicting the structural response in shear loading, a single-edge notched (SEN) concrete beam of Arrea and Ingraffea [73] was used for the numerical verification. The geometry of the SEN concrete beam, boundary, and four-point shear loading conditions, which were used to induce a mixed tensile/shear failure, are shown in Figure 14. The load was applied using a steel beam, through which the load was transmitted to the SEN concrete beam at points A and B (Figure 14).

The material properties of the SEN beam used in the analysis were Young’s modulus $E_0 = 2.48 \times 10^4$ MPa, Poisson’s ratio $\nu_0 = 0.18$, concrete uniaxial tensile strength $f_t = 3.5$ MPa, $A_t = 1.0$, uniaxial compressive strength $f_c = 35.0$ MPa, $\gamma = 2.2$, Mode-I fracture energy $G_t^I = 0.075$ N/mm, and compressive fracture energy $G_c^c = 15.0$ N/mm. The steel plates used as load distributors

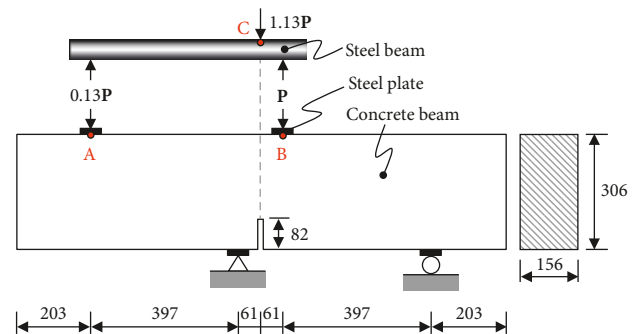


FIGURE 14: SEN concrete beam: geometry, boundary, and loading conditions (dimensions in mm).

were assumed to be a linear elastic material with Young’s modulus $E_s = 210$ GPa and Poisson’s ratio $\nu_s = 0.3$.

The SEN concrete beam and the steel plates were discretized by four-node quadrilateral (with 2×2 Gaussian

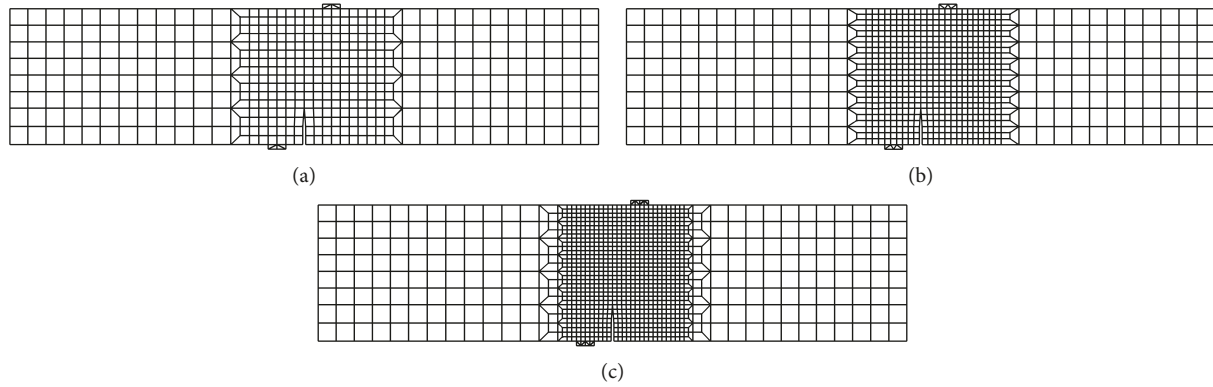


FIGURE 15: Different FE mesh sizes for the SEN concrete beam in the mesh-size dependency study: (a) coarse mesh; (b) medium mesh; (c) fine mesh.

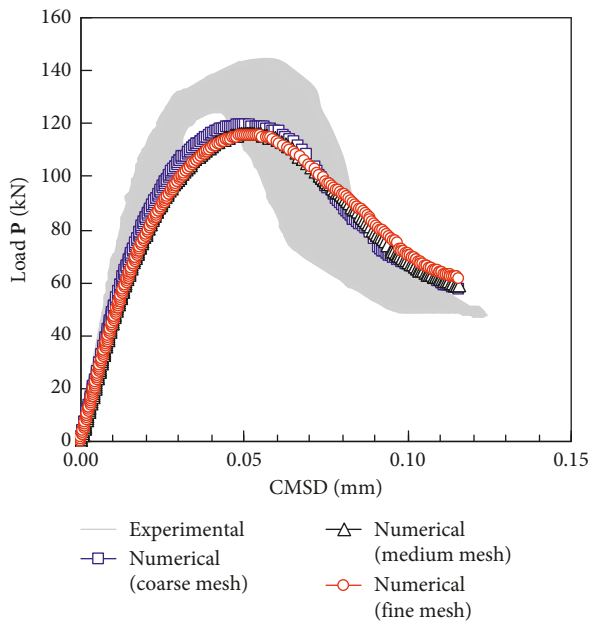


FIGURE 16: Load-CMSD curves for SEN concrete beam obtained with different FE mesh sizes.

integration) and three-node triangular plane stress elements in the FE analysis, respectively. Three different mesh sizes were used for the mesh-size dependency study: coarse, medium, and fine meshes, which had a total of 480, 810, and 1176 elements, respectively (Figure 15). The corresponding minimum element sizes of these three meshes were 19.1 mm, 12.8 mm, and 9.6 mm, respectively.

Figure 16 presents the predicted structural responses in terms of the load P at point B versus the crack mouth sliding displacement (CMSD). Figure 17 shows the simulated final tensile damage distribution, which is denoted by the dark color corresponding to a high damage value close to one. Figure 18 shows the simulated crack patterns at the final computation stage.

According to the numerical results, it is clear that (i) the global structural responses are well predicted compared to the experimental results (Figure 16); (ii) the proposed model

provides an acceptable prediction of the curved macroscopic crack, as compared with the experimentally observed crack trajectory (Figures 17 and 18); and (iii) the simulated crack trajectories obtained with the medium and fine meshes are identical, which indicates that the predicted paths of the crack propagation are almost mesh-size independent.

The predicted thicknesses of the macroscopic crack are inconsistent when using different mesh sizes, as shown in Figures 17 and 18. As more clearly shown in Figure 18, the simulated localization band tends to occur in one row of elements. This is due to the inherent deficiency of the crack band approach since the rate BVP still remains ill-posed [63]. The similar conclusion to simulations with low-order elements can be found in the study of Jirásek and Bauer [59], who also pointed out that the minimum size of the localization band is the size of one row of integration points (i.e., subelement domains) but not the size of one row of elements in simulations with high-order elements.

As also can be observed in Figures 17 and 18, the predicted crack trajectories are less curved than its experimental counterpart due to the approximation error of the spatial discretization in the standard finite element method. It can be explained by the fact that the localized damage zone cannot be resolved with sufficient accuracy because of the minimum element size (19.1 mm) of the coarse mesh being too large, as compared with the thickness of the notch (5 mm).

4. Conclusions

This paper presents a tension-compression damage model with consistent crack bandwidths developed for the macroscopic description of concrete behaviors. The model is formulated within the framework of the internal variable theory of thermodynamics so that the constitutive relations are derived without ad hoc assumptions. Based on the numerical and experimental results, the following conclusions can be drawn:

- (i) The essential features of the proposed model include the identification of tensile/compressive strain states by the sign of the volumetric deformation, the

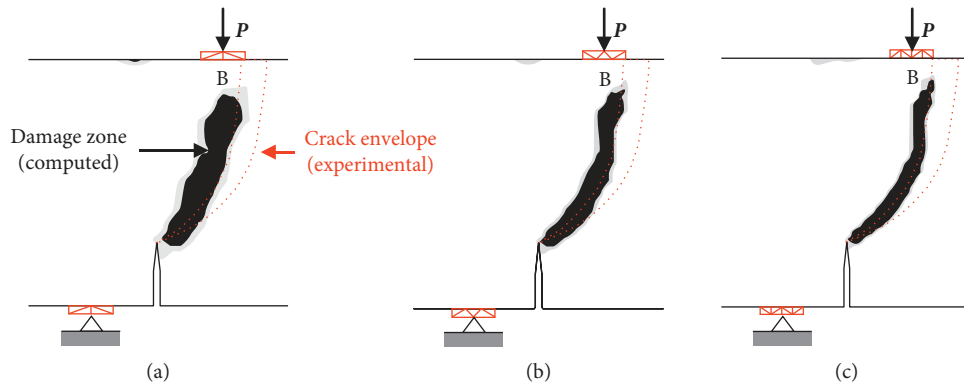


FIGURE 17: Final tensile damage profiles in the central part of the SEN concrete beam: (a) coarse mesh; (b) medium mesh; (c) fine mesh.

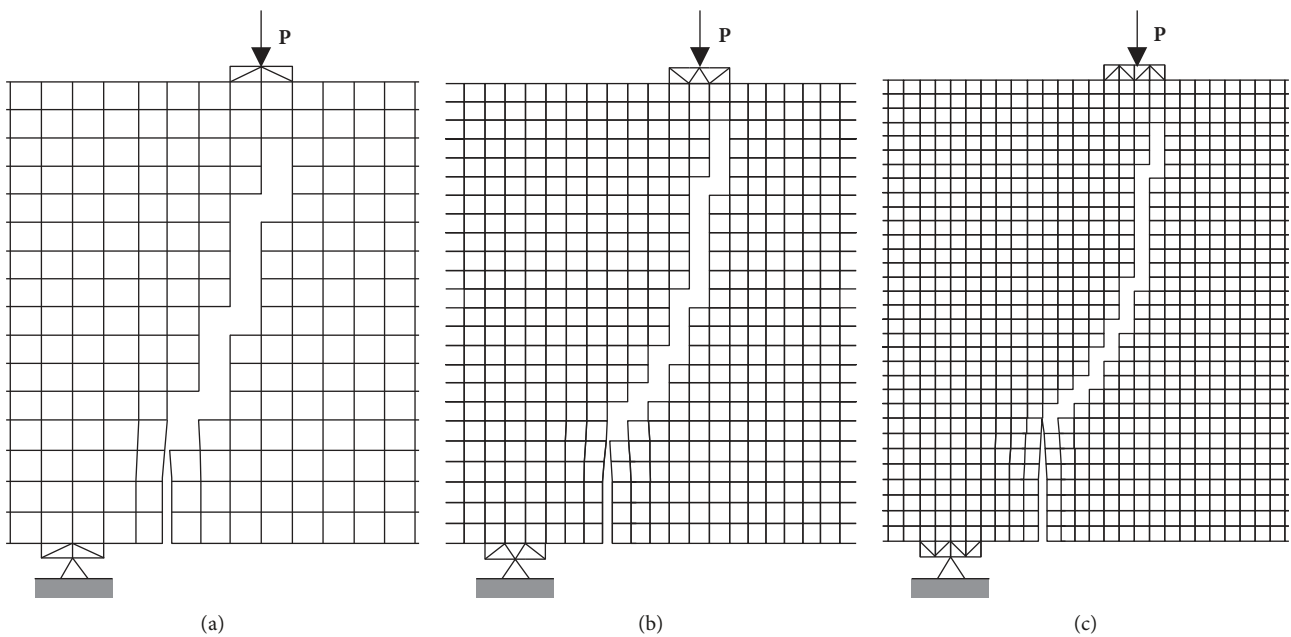


FIGURE 18: Computed final crack patterns in the central part of the SEN concrete beam: (a) coarse mesh; (b) medium mesh; (c) fine mesh.

rational definition of two equivalent strains, two internal variables, and two separated damage criteria describing distinct damage mechanics under tension and compression. Such features enable the present model to provide a better prediction of the distinct tension-compression behaviors of concrete materials. Furthermore, the adopted method using the sign of the volumetric deformation avoids the premature convergence difficult in the numerical analysis, which is often encountered in existing models using the spectral decomposition of a stress or strain tensor.

(ii) The main contribution of this paper is that it provides an improved estimation of the crack bandwidth, which is developed for two-dimensional linear elements by taking into account the element shape, element size, and element orientation with

respect to crack directions and spatial positions. Its capability in numerical analyses of irregular meshes and arbitrary crack directions has been validated by the comparative study of existing estimations of the crack bandwidth at the element level. The proposed model incorporating this enhanced description of the crack bandwidth has also been proven to be mesh-size independent at the structural level. The present model is able to provide objective simulation results with respect to the finite element mesh refinements that are very important for the computation of the real engineering structures.

(iii) The proposed model has been validated by the well-documented experimental data of concrete. The good agreement between the predicted and experimental results consequently demonstrates that the present model provides an effective tool for

modeling concrete behaviors in tension and compression.

- (iv) The present model has a limited number of material parameters, each of which has a clear physical meaning and can be identified by standard laboratory tests. Moreover, the simplicity and the explicit integration of the constitutive equations make the model well suited for large-scale computations.

Data Availability

The data used to support the findings of this study are included within the article.

Conflicts of Interest

The authors declare that they have no conflicts of interest.

Acknowledgments

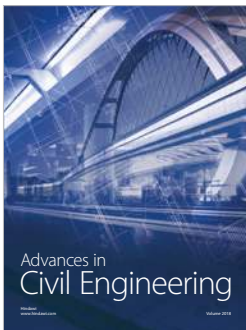
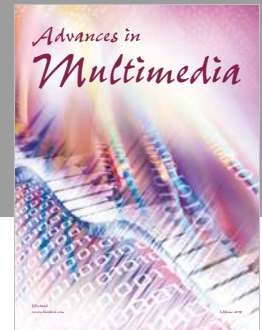
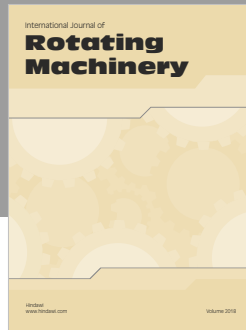
The work described in this paper was supported by the National Natural Science Foundation of China (51208005), the Transportation Science Research Project of Jiangsu Province (0213Y25), the Natural Science Foundation of Anhui Province of China (1208085QE80), the Educational Department of Anhui Province of China (KJ2012A095), and the Doctoral Fund of Anhui University of Science & Technology (11084).

References

- [1] L. K. Turner and F. G. Collins, "Carbon dioxide equivalent (CO₂-e) emissions: a comparison between geopolymer and OPC cement concrete," *Construction and Building Materials*, vol. 43, pp. 125–130, 2013.
- [2] Z.-D. Xu and Z. Wu, "Energy damage detection strategy based on acceleration responses for long-span bridge structures," *Engineering Structures*, vol. 29, no. 4, pp. 609–617, 2007.
- [3] S. Yazdani, "On a class of continuum damage mechanics theories," *International Journal of Damage Mechanics*, vol. 2, no. 2, pp. 162–176, 2016.
- [4] C. Goidescu, H. Welemane, O. Pantalé, M. Karama, and D. Kondo, "Anisotropic unilateral damage with initial orthotropy: a micromechanics-based approach," *International Journal of Damage Mechanics*, vol. 24, no. 3, pp. 313–337, 2014.
- [5] J. Mazars, "A description of micro- and macroscale damage of concrete structures," *Engineering Fracture Mechanics*, vol. 25, no. 5–6, pp. 729–737, 1986.
- [6] G. Pijaudier-Cabot and Z. P. Bažant, "Nonlocal damage theory," *Journal of Engineering Mechanics*, vol. 113, pp. 1512–1533, 1987.
- [7] J. C. Simo and J. W. Ju, "Strain- and stress-based continuum damage models-I. Formulation," *International Journal of Solids and Structures*, vol. 23, no. 7, pp. 821–840, 1987.
- [8] D. Krajcinovic, "Damage mechanics," *Mechanics of Materials*, vol. 8, no. 2–3, pp. 117–197, 1989.
- [9] G. Z. Voyiadjis and T. M. Abu-Lebdeh, "Damage model for concrete using bounding surface concept," *Journal of Engineering Mechanics*, vol. 119, no. 9, pp. 1865–1885, 1993.
- [10] J. L. Chaboche, P. M. Lesne, and J. F. Maire, "Continuum damage mechanics, anisotropy and damage deactivation for brittle materials like concrete and ceramic composites," *International Journal of Damage Mechanics*, vol. 4, no. 1, pp. 5–22, 2016.
- [11] M. Cervera, J. Oliver, and O. Manzoli, "A rate-dependent isotropic damage model for the seismic analysis of concrete dams," *Earthquake Engineering & Structural Dynamics*, vol. 25, no. 9, pp. 987–1010, 1996.
- [12] S. Murakami and K. Kamiya, "Constitutive and damage evolution equations of elastic-brittle materials based on irreversible thermodynamics," *International Journal of Mechanical Sciences*, vol. 39, no. 4, pp. 473–486, 1997.
- [13] R. H. J. Peerlings, R. de Borst, W. A. M. Brekelmans, and M. G. D. Geers, "Gradient-enhanced damage modelling of concrete fracture," *Mechanics of Cohesive-frictional Materials*, vol. 3, no. 4, pp. 323–342, 1998.
- [14] N. Xie, Q.-Z. Zhu, J.-F. Shao, and L.-H. Xu, "Micromechanical analysis of damage in saturated quasi brittle materials," *International Journal of Solids and Structures*, vol. 49, no. 6, pp. 919–928, 2012.
- [15] J. J. C. Pituba and G. R. Fernandes, "Anisotropic damage model for concrete," *Journal of Engineering Mechanics*, vol. 137, no. 9, pp. 610–624, 2011.
- [16] S. Zhu and C. Cai, "Stress intensity factors evaluation for through-transverse crack in slab track system under vehicle dynamic load," *Engineering Failure Analysis*, vol. 46, pp. 219–237, 2014.
- [17] S. Zhu, Q. Fu, C. Cai, and P. D. Spanos, "Damage evolution and dynamic response of cement asphalt mortar layer of slab track under vehicle dynamic load," *Science China Technological Sciences*, vol. 57, no. 10, pp. 1883–1894, 2014.
- [18] B. Valentini and G. Hofstetter, "Review and enhancement of 3D concrete models for large-scale numerical simulations of concrete structures," *International Journal for Numerical and Analytical Methods in Geomechanics*, vol. 37, no. 3, pp. 221–246, 2013.
- [19] C. Wen and S. Yazdani, "Anisotropic damage model for woven fabric composites during tension-tension fatigue," *Composite Structures*, vol. 82, no. 1, pp. 127–131, 2008.
- [20] L. Pelà, M. Cervera, and P. Roca, "An orthotropic damage model for the analysis of masonry structures," *Construction and Building Materials*, vol. 41, pp. 957–967, 2013.
- [21] A. Khennane, M. Khelifa, L. Bleron, and J. Viguier, "Numerical modelling of ductile damage evolution in tensile and bending tests of timber structures," *Mechanics of Materials*, vol. 68, pp. 228–236, 2014.
- [22] G. Z. Voyiadjis and P. I. Kattan, "Mechanics of small damage in fiber-reinforced composite materials," *Composite Structures*, vol. 92, no. 9, pp. 2187–2193, 2010.
- [23] M. Ganjiani, R. Naghdabadi, and M. Asghari, "Analysis of concrete pressure vessels in the framework of continuum damage mechanics," *International Journal of Damage Mechanics*, vol. 21, no. 6, pp. 843–870, 2011.
- [24] A. Sellier, G. Casaux-Ginestet, L. Buffo-Lacarrière, and X. Bourbon, "Orthotropic damage coupled with localized crack reclosure processing. Part I: constitutive laws," *Engineering Fracture Mechanics*, vol. 97, pp. 148–167, 2013.
- [25] X. Tao and D. V. Phillips, "A simplified isotropic damage model for concrete under bi-axial stress states," *Cement and Concrete Composites*, vol. 27, no. 6, pp. 716–726, 2005.
- [26] C. Comi and U. Perego, "Fracture energy based bi-dissipative damage model for concrete," *International Journal of Solids and Structures*, vol. 38, no. 36–37, pp. 6427–6454, 2001.
- [27] J. H. P. de Vree, W. A. M. Brekelmans, and M. A. J. van Gils, "Comparison of nonlocal approaches in continuum damage

- mechanics,” *Computers and Structures*, vol. 55, no. 4, pp. 581–588, 1995.
- [28] A. Pros, P. Díez, and C. Molins, “Numerical modeling of the double punch test for plain concrete,” *International Journal of Solids and Structures*, vol. 48, no. 7–8, pp. 1229–1238, 2011.
- [29] P. E. Bernard, N. Moës, and N. Chevaugeon, “Damage growth modeling using the thick level set (TLS) approach: efficient discretization for quasi-static loadings,” *Computer Methods in Applied Mechanics and Engineering*, vol. 233–236, pp. 11–27, 2012.
- [30] S. Y. Alam, P. Kotronis, and A. Loukili, “Crack propagation and size effect in concrete using a non-local damage model,” *Engineering Fracture Mechanics*, vol. 109, pp. 246–261, 2013.
- [31] S. Saroukhani, R. Vafadari, and A. Simone, “A simplified implementation of a gradient-enhanced damage model with transient length scale effects,” *Computational Mechanics*, vol. 51, no. 6, pp. 899–909, 2012.
- [32] G. Sciumè, F. Benboudjema, C. De Sa, F. Pesavento, Y. Berthaud, and B. A. Schrefler, “A multiphysics model for concrete at early age applied to repairs problems,” *Engineering Structures*, vol. 57, pp. 374–387, 2013.
- [33] Z. P. Bažant and B. H. Oh, “Crack band theory for fracture of concrete,” *Materials and Structures*, vol. 16, no. 3, pp. 155–177, 1983.
- [34] M. Cervera, L. Pelà, R. Clemente, and P. Roca, “A crack-tracking technique for localized damage in quasi-brittle materials,” *Engineering Fracture Mechanics*, vol. 77, no. 13, pp. 2431–2450, 2010.
- [35] R. de Borst, L. J. Sluys, H. B. Muhlhaus, and J. Pamin, “Fundamental issues in finite element analyses of localization of deformation,” *Engineering Computations*, vol. 10, no. 2, pp. 99–121, 1993.
- [36] J. Oliver, A. E. Huespe, and I. F. Dias, “Strain localization, strong discontinuities and material fracture: matches and mismatches,” *Computer Methods in Applied Mechanics and Engineering*, vol. 241–244, pp. 323–336, 2012.
- [37] Z. P. Bažant and M. Jirásek, “Nonlocal integral formulations of plasticity and damage: survey of progress,” *Journal of Engineering Mechanics*, vol. 128, no. 11, pp. 1119–1149, 2002.
- [38] M. Cervera, M. Chiumenti, and R. Codina, “Mixed stabilized finite element methods in nonlinear solid mechanics: Part I: formulation,” *Computer Methods in Applied Mechanics and Engineering*, vol. 199, no. 37–40, pp. 2559–2570, 2010.
- [39] M. Cervera, M. Chiumenti, and R. Codina, “Mixed stabilized finite element methods in nonlinear solid mechanics: Part II: strain localization,” *Computer Methods in Applied Mechanics and Engineering*, vol. 199, no. 37–40, pp. 2571–2589, 2010.
- [40] M. Cervera and M. Chiumenti, “Smearred crack approach: back to the original track,” *International Journal for Numerical and Analytical Methods in Geomechanics*, vol. 30, no. 12, pp. 1173–1199, 2006.
- [41] W. He, Y.-F. Wu, K. M. Liew, and Z. Wu, “A 2D total strain based constitutive model for predicting the behaviors of concrete structures,” *International Journal of Engineering Science*, vol. 44, no. 18–19, pp. 1280–1303, 2006.
- [42] L. Pelà, M. Cervera, S. Oller, and M. Chiumenti, “A localized mapped damage model for orthotropic materials,” *Engineering Fracture Mechanics*, vol. 124–125, pp. 196–216, 2014.
- [43] M. Jirásek and S. Marfia, “Non-local damage model based on displacement averaging,” *International Journal for Numerical Methods in Engineering*, vol. 63, no. 1, pp. 77–102, 2005.
- [44] W. He, Y.-F. Wu, Y. Xu, and T.-T. Fu, “A thermodynamically consistent nonlocal damage model for concrete materials with unilateral effects,” *Computer Methods in Applied Mechanics and Engineering*, vol. 297, pp. 371–391, 2015.
- [45] R. K. Abu Al-Rub and G. Z. Voyiadjis, “Gradient-enhanced coupled plasticity-anisotropic damage model for concrete fracture: computational aspects and applications,” *International Journal of Damage Mechanics*, vol. 18, no. 2, pp. 115–154, 2009.
- [46] R. de Borst and L. J. Sluys, “Localisation in a Cosserat continuum under static and dynamic loading conditions,” *Computer Methods in Applied Mechanics and Engineering*, vol. 90, no. 1–3, pp. 805–827, 1991.
- [47] C. Giry, C. Oliver-Leblond, F. Dufour, and F. Ragueneau, “Cracking analysis of reinforced concrete structures,” *European Journal of Environmental and Civil Engineering*, vol. 18, no. 7, pp. 724–737, 2014.
- [48] A. Simone, H. Askes, and L. J. Sluys, “Incorrect initiation and propagation of failure in non-local and gradient-enhanced media,” *International Journal of Solids and Structures*, vol. 41, no. 2, pp. 351–363, 2004.
- [49] M. Jirásek, S. Rolshoven, and P. Grassl, “Size effect on fracture energy induced by non-locality,” *International Journal for Numerical and Analytical Methods in Geomechanics*, vol. 28, no. 78, pp. 653–670, 2004.
- [50] K. Haidar, J. F. Dubé, and G. Pijaudier-Cabot, “Modelling crack propagation in concrete structures with a two scale approach,” *International Journal for Numerical and Analytical Methods in Geomechanics*, vol. 27, no. 13, pp. 1187–1205, 2003.
- [51] J. A. Paredes, A. H. Barbat, and S. Oller, “A compression-tension concrete damage model, applied to a wind turbine reinforced concrete tower,” *Engineering Structures*, vol. 33, no. 12, pp. 3559–3569, 2011.
- [52] M. Alembagheri and M. Ghaemian, “Incremental dynamic analysis of concrete gravity dams including base and lift joints,” *Earthquake Engineering and Engineering Vibration*, vol. 12, no. 1, pp. 119–134, 2013.
- [53] J. G. Rots, *Computational modeling of concrete fracture*, Ph.D. thesis, Delft University of Technology, Delft, the Netherlands, 1988.
- [54] P. H. Feenstra and R. de Borst, “Constitutive model for reinforced concrete,” *Journal of Engineering Mechanics*, vol. 121, no. 5, pp. 587–595, 1995.
- [55] R. Scotta, R. Vitaliani, A. Saetta, E. Oñate, and A. Hanganu, “A scalar damage model with a shear retention factor for the analysis of reinforced concrete structures: theory and validation,” *Computers and structures*, vol. 79, no. 7, pp. 737–755, 2001.
- [56] J. Oliver, “A consistent characteristic length for smeared cracking models,” *International Journal for Numerical Methods in Engineering*, vol. 28, no. 2, pp. 461–474, 1989.
- [57] V. Červenka, R. Pukl, J. Ožbold, and R. Eligehausen, “Mesh sensitivity effects in smeared finite element analysis of concrete fracture,” in *Fracture Mechanics of Concrete Structures*, F. H. Wittmann, Ed., pp. 1387–1396, Aedificatio Publishers, Freiburg, Germany, 1995.
- [58] S. Govindjee, G. J. Kay, and J. C. Simo, “Anisotropic modelling and numerical simulation of brittle damage in concrete,” *International Journal for Numerical Methods in Engineering*, vol. 38, no. 21, pp. 3611–3633, 1995.
- [59] M. Jirásek and M. Bauer, “Numerical aspects of the crack band approach,” *Computers and Structures*, vol. 110–111, pp. 60–78, 2012.
- [60] A. T. Slobbe, M. A. N. Hendriks, and J. G. Rots, “Systematic assessment of directional mesh bias with periodic boundary

- conditions: applied to the crack band model,” *Engineering Fracture Mechanics*, vol. 109, pp. 186–208, 2013.
- [61] C. Comi, “A non-local model with tension and compression damage mechanisms,” *European Journal of Mechanics-A/Solids*, vol. 20, no. 1, pp. 1–22, 2001.
- [62] M. Jirásek and P. Grassl, “Evaluation of directional mesh bias in concrete fracture simulations using continuum damage models,” *Engineering Fracture Mechanics*, vol. 75, no. 8, pp. 1921–1943, 2008.
- [63] R. de Borst, “Some recent developments in computational modelling of concrete fracture,” *International Journal of Fracture*, vol. 86, no. 1-2, pp. 5–36, 1997.
- [64] I. Carol and K. Willam, “Spurious energy dissipation/generation in stiffness recovery models for elastic degradation and damage,” *International Journal of Solids and Structures*, vol. 33, no. 20–22, pp. 2939–2957, 1996.
- [65] J. W. Ju, “On energy-based coupled elastoplastic damage theories: constitutive modeling and computational aspects,” *International Journal of Solids and Structures*, vol. 25, no. 7, pp. 803–833, 1989.
- [66] R. Faria, J. Oliver, and M. Cervera, “A strain-based plastic viscous-damage model for massive concrete structures,” *International Journal of Solids and Structures*, vol. 35, no. 14, pp. 1533–1558, 1998.
- [67] J. Y. Wu, J. Li, and R. Faria, “An energy release rate-based plastic-damage model for concrete,” *International Journal of Solids and Structures*, vol. 43, no. 3-4, pp. 583–612, 2006.
- [68] S. Fichant, C. La Borderie, and G. Pijaudier-Cabot, “Isotropic and anisotropic descriptions of damage in concrete structures,” *Mechanics of Cohesive-frictional Materials*, vol. 4, no. 4, pp. 339–359, 1999.
- [69] H. Kupfer, H. K. Hilsdorf, and H. Rusch, “Behavior of concrete under biaxial stresses,” *ACI Journal*, vol. 66, no. 8, pp. 656–666, 1969.
- [70] R. K. Abu Al-Rub and S.-M. Kim, “Computational applications of a coupled plasticity-damage constitutive model for simulating plain concrete fracture,” *Engineering Fracture Mechanics*, vol. 77, no. 10, pp. 1577–1603, 2010.
- [71] G. Z. Voyiadjis, Z. N. Taqieddin, and P. I. Kattan, “Theoretical formulation of a coupled elastic-plastic anisotropic damage model for concrete using the strain energy equivalence concept,” *International Journal of Damage Mechanics*, vol. 18, no. 7, pp. 603–638, 2008.
- [72] D. A. Hordijk, *Local approach to fatigue of concrete*, Ph.D. thesis, Delft University of Technology, Delft, The Netherlands, 1991.
- [73] M. Arrea and A. R. Ingraffea, *Mixed-Mode Crack Propagation in Mortar and Concrete*, Department of Structural Engineering, Cornell University, Ithaca, NY, USA, 1982.



Hindawi

Submit your manuscripts at
www.hindawi.com

